Evolution of Gradual and Abrupt Trends in Nighttime Lights and Responses to Land Drivers via BFAST01 and Geographically Weighted Regression

Biyun Guo, Deyong Hu, Zongyao Wang, and Aixuan Lin

***Abstract*—Nighttime lights (NTLs) provide an unparalleled view for understanding urban environments. The high-frequency NTL intensity changes (NTLICs) and their land drivers in megaregions are less investigated. Here, monthly Visible Infrared Imaging Radiometer Suite-Day Night Band (VIIRS-DNB) NTL images from 2014 to 2020 were regarded as time series modeling input data. Furthermore, the 7-year mean values of five types of Points of Interest Density (POID), Road Density (RD), Normalized Difference Vegetation Index (NDVI), and Normalized Difference Built-up Index (NDBI) were used to extract features as land drivers of NTLIC. A simplified version of the Breaks For Additive Season and Trend (BFAST01) algorithm was adopted to detect major changes in monthly NTL intensity at the pixel level in the Beijing–Tianjin–Hebei (BTH) megaregion, China. Geographically weighted regression (GWR) was used to address the spatial nonstationarity of the land drivers. The results showed that (1) increasing trends (63.35%) and decreasing trends (4.57%) were mainly observed in central and coastal cities, respectively. This indicates that the spatial characteristics of the NLTIC were unbalanced; (2) reversal change type 8 (37.29% of abrupt changes) was the dominant type, mainly occurring around April 2017, which may be related to the non-capital function redistribution policy; (3) NDVI and RD were the best one of two physical drivers and six human activity drivers, respectively; and (4) the R^2 of the GWR reached 0.60, a 20% improvement over ordinary least squares regression. This study provides an insightful understanding of the dynamics of NTL intensity and its response mechanisms in megaregions.**

***Index Terms*—BFAST01, geographically weighted regression (GWR), land drivers, nighttime lights (NTLs), urbanization.**

I. Introduction

NIGHTTIME lights (NTLs) from space offer a helpful view in describing the extent and intensity of urbanization [1], [2]. It also has close relationships with land use (LU), land cover (LC), human activities, and energy consumption patterns [3], [4], [5]. Thus, NTL imagery originating from satellites such as the defense meteorological satellite program—operational linescan system (DMSP-OLS) and visible infrared imaging radiometer suite—day night band (VIIRS-DNB) have been widely used in urban research. These NTL data have been used to characterize urbanization features, i.e., urban extent [6], [7], population density [8], [9], and socioeconomic activities [10], [11].

Urban studies based on NTL data have obvious advantages over daytime multispectral datasets, i.e., Landsat and Sentinel imagery. These advantages include reflecting a comprehensive degree of urbanization, high computational efficiency, broad spatial coverage, and a relatively long temporal span [6], [12], [13]. Time-series NTL analysis based on multitemporal products has recently received more attention due to the availability of high-frequency data [2], [14] and the power of long-range NTL trajectories [6], [13]. In addition, rapid changes in urban areas have become widespread, profoundly affecting the intensity and extent of NTL [7]. Therefore, it is beneficial to understand urban changes at night using the time series analysis of NTL to gain knowledge of the NTL intensity change (NTLIC) in terms of where, when, direction, and magnitude.

Two types of studies can be divided based on the two temporal composite NTL products. The DMSP-OLS stable version 4 annual composite products have been widely used to extract urban area [6], [13], estimate population density [8], [9], and investigate urban dynamics at the global scale [13]. In contrast, there were more advantages in the monthly VIIRS-DNB composite NTL products, i.e., consistency in time series, higher frequency observations, and fewer data problems in saturation and blooming than the DMSP-OLS NTL data [2], [15]. Urban studies based on VIIRS-DNB NTL not only focus on urbanization dynamics [7], [16], but also pay close attention to NTL seasonality [3], [17] and the impact of short-term events, i.e., hurricanes [18], war conflicts [19], COVID-19 [20], and special festivals [21], [22], on urban economic development. This means that monthly composite NTL data can provide new insights into the urban environment, which is highly dynamic and undergoes gradual and abrupt changes [1], [14], and deliver relevant and timely information for urban response and management. However, major NTLIC, including gradual and abrupt trends, have not been thoroughly investigated.

To date, advances in change detection have been made through time series analysis techniques, with various models proposed to segment the time series into different components, such as

Manuscript received 26 April 2023; revised 6 July 2023 and 14 August 2023; accepted 6 September 2023. Date of publication 11 September 2023; date of current version 25 September 2023. This work was supported by the National Natural Science Foundation of China under Grant 41671339. *(Corresponding author: Deyong Hu.)*

The authors are with the College of Resource Environment and Tourism, Capital Normal University, Beijing 100048, China, and also with the Key Laboratory of 3D Information Acquisition and Application, Ministry of Education, Capital Normal University, Beijing 100048, China (e-mail: biyunguo@cnu.edu.cn; deyonghu@cnu.edu.cn; 2210902133@cnu.edu.cn; 2210902099@cnu.edu.cn).

Digital Object Identifier 10.1109/JSTARS.2023.3314087

This work is licensed under a Creative Commons Attribution-NonCommercial-NoDerivatives 4.0 License. For more information, see https://creativecommons.org/licenses/by-nc-nd/4.0/

BFAST [23], LandTrendr [24], and CCDC [25]. These methods could detect gradual and abrupt changes, but their computation was intensive, and the breakpoints included some small structural changes [26]. These limitations make it difficult to accurately detect the major changes in NTL. De Jong et al. (2013) proposed a model named BFAST01 to detect major (gradual and abrupt) changes in vegetation activity trends, their associated types (four monotonic changes, two interruptions, and two reversals), timing, and magnitude [27]. The BFAST01 algorithm has been used to detect the changes in temperature trends [28] and aerosol vertical distribution [29] at national and regional scales, respectively. In addition, the BFAST model has been used to decompose the components of time-series NTL [30] at the national level. Therefore, BFAST01 has the potential to efficiently detect major (abrupt and gradual) changes in the monthly composite NTL intensity.

Some researchers have studied the causes of the observed NTL intensity. The relationships between NTL intensity and features of LC, LU, and human activities at the pixel and parcel scales have been investigated using various methods, including statistical index, random forest, stepwise multiple regression, unmixing model, and multiscale geographically weighted regression (GWR) model [3], [17], [31], [32], [33], [34]. These studies have demonstrated the relationships between the NTL intensity and land features at a finer scale. However, few studies have investigated the spatial heterogeneity of the response processes between the NTLIC and land drivers at the pixel level. Many studies have found that the normalized difference vegetation index (NDVI) and road density (RD), which are used to describe the condition of vegetation and roads, are important factors influencing NTL [35], [36]. Nevertheless, the specific relationship between the NTLIC and these two land drivers has not been identified from the perspective of spatial nonstationary characteristics. Therefore, it is meaningful to fill this gap and clarify the causes of NTLIC.

Because of the wide coverage and high frequency of VIIRS-DNB NTL products, they were selected to detect the abrupt and gradual changes in time series NTL in the megaregion. The significance of the megaregion is presented as follows: (i) it includes multiple cities with different sizes, forms, functions and urbanization degrees; (ii) the interactions between two cities are closed due to the strategy of harmonious regional development; and (iii) its development is crucial for urban sustainability [37]. In the context of new urbanization, the Beijing–Tianjin–Hebei (BTH) megaregion has received much attention in China. Previous studies have mainly focused on the impacts of urbanization on the natural environment [38], sustainable development [37], [39], and landscape changes [40]. However, the NTLIC caused by the urbanization process has not been thoroughly investigated. Therefore, it is imperative to reveal changes in monthly NTL intensity in time series to further understand the process of change in urban megaregions.

To comprehensively understand the gradual and abrupt changes in the time-series monthly NTL in the urban megaregion, the BFAST01 model was applied to detect NTLIC using the monthly VIIRS-DNB NTL products in the BTH megaregion of China from 2014 to 2020. Then, we analyzed the primary land drivers of the spatiotemporal evolution of NTL trends and validated the applicability of GWR to clarify the mechanisms of NTLIC.

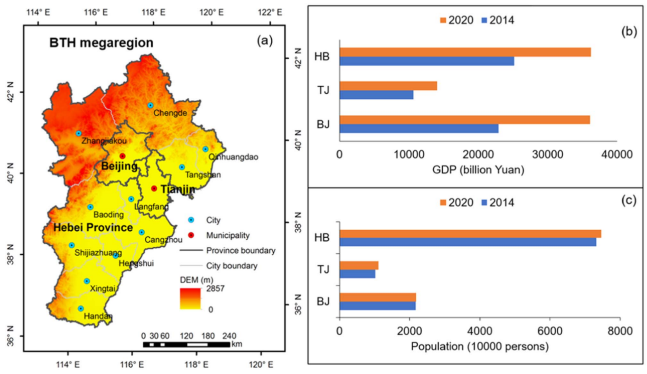

Fig. 1. (a) Physical and (b-c) socio-economic conditions of the Beijing (BJ)-Tianjin (TJ)-Hebei (HB) megaregion. HB province includes 11 cities, e.g., Chengde, Zhangjiakou, Qinhuangdao, Langfang, Tangshan, Baoding, Cangzhou, Shijiazhuang, Hengshui, Xingtai, and Handan.

II. Study Area and Data

A. Study Area

The BTH urban megaregion plays an essential role in China due to its political, cultural and economic functions. The BTH megaregion is located in northern China and covers an area of approximately 215800 km^2, consisting of Beijing Municipality, Tianjin Municipality and Hebei Province (see Fig. 1). Its environment is complex and diverse, with high elevations in the northwestern areas and plains in the central areas [see Fig. 1(a)]. Meanwhile, it shows apparent changes in gross domestic product (GDP) but small changes in population from 2014 to 2020, especially in Beijing [see Fig. 1(b) and (c)]. This may be related to the national strategy to relieve non-capital functions in Beijing, control population growth, and regulate industrial structure [41]. Therefore, the intensity of socioeconomic activities has been deeply affected. Hence, the NTL intensity in the BTH megaregion will change significantly during this period.

B. Data and Preprocessing

Remote sensing imagery, multisource geospatial data, and statistical data were the primary data sources (see Table I). The remote sensing data included VIIRS-DNB NTL and MODIS data. VIIRS-DNB NTL data were downloaded from the Earth Observation Group, and MODIS data were obtained from the Google Earth Engine platform. Preprocessing steps included resampling to 500 m spatial resolution and projection transformation to Albers Equal Area Projection.

The version 1 monthly cloud-free VIIRS-DNB NTL composites from January 2014 to December 2020, a total of 84 scene images, were the primary data used to detect NTL changes. The "vcmsl" (corrected for stray light-contaminated data) version of the monthly composites was selected because of its broader spatial coverage than the "vcm" version. The VIIRS-DNB NTL image has a spatial resolution of 500 m, a radiometric resolution

TABLE I
BASIC INFORMATION ABOUT THE DATASETS

Data	Number	Spatial resolution	Temporal range	Source
Monthly VIIRS-DNB NTL (vcmsl)	84	500 m	2014-2020	https://eogdata.mines.edu/products/vnl/#monthly
Annual VNL V2-NPP lit-mask	7	500 m	2014-2020	https://eogdata.mines.edu/nighttime_light/annual/v20/
MOD13A1 V6-NDVI MCD43A4-B2, B7	168	500 m	2014-2020	Google earth engine
Road and POI	-	-	2014-2020	Open street map
GDP and the total permanent population	-	-	2014-2020	National Bureau of Statistics

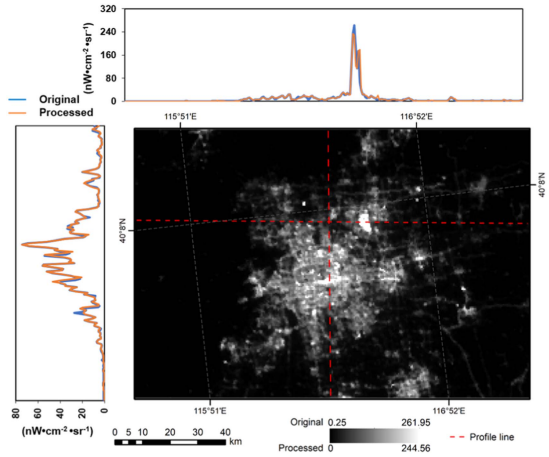

Fig. 2. Profiles of the original and processed VIIRS-DNB NTL in May 2020.

of 14 bit, and a sensitive low light detection limit (2×10^{-11} $W \cdot cm^{-2} \cdot sr^{-1}$) [42].

The abnormal and background noise needs to be smoothed because the monthly composites have not been filtered out of temporary lights (e.g., auroras and fires). A method combining a background mask and a local median filter was developed to achieve this goal. First, all non-zero pixels for possible temporary lights and background noise in the monthly images were identified using the version 2 annual lit mask data per year [43] and then replaced with values of zero. Therefore, these areas were non-lit pixels that were not involved in the subsequent process. Second, high-intensity human activity areas, including airports, commercial areas, and entertainment areas, were selected to identify high thresholds in each month. Third, a median filter was applied to the regions with pixel values greater than this threshold. Fig. 2 shows that the processed VIIRS-DNB NTL time series removes abnormally high and low observations while preserving their overall trends.

The other remote sensing data were standard products from the MODIS data library. We chose the NDVI and Normalized Difference Built-up Index (NDBI) to describe the spatial extent and intensity of vegetation cover and built-up areas, respectively. NDVI was derived from the NDVI layer of the MOD13A1 image with a spatial resolution of 500 m and a temporal resolution of 16 days. NDBI was generated from the surface reflectance (SR) layer of the MCD43A4 image using the near-infrared (NIR) and mid-infrared (MIR) bands, as shown in (1). These two spectral indices were used to describe the state of the LC

$$\mathrm{NDBI} = (\mathrm{MIR} - \mathrm{NIR}) / (\mathrm{MIR} + \mathrm{NIR}) \tag{1}$$

Multisource geospatial datasets include road and points of interest (POI) vector data. They were used to represent the intensity of human activity in various LU types. These two datasets were collected from the Open Street Map between 2014 and 2020. To better analyze the changes in human activities, the POI datasets were reclassified into five types [44], including residential land, commercial land, industrial land, public management and public service land, and greenspaces. The statistical data, i.e., the total permanent population and GDP, were used to describe the socioeconomic conditions of each city in the BTH megaregion.

III. METHODOLOGY

This article focused on testing and modeling the periodicity and process of NTLIC. To achieve this objective, the Lomb-Scargle periodogram test was used to judge and identify the periodicity of NTL. The BFAST01 model was used to fit monthly VIIRS-DNB time series and characterize the NTLIC, including the type, timing, and significance of gradual and abrupt changes, the magnitude of abrupt changes, the fitted NTL, and the root mean square error (*RMSE*) of the fitted NTL. This means that the gradual and abrupt change features of NTL intensity could be analyzed at the pixel level. Second, the potential factors affecting NTL in terms of LC and LU conditions were extracted, and then the most important factors were identified by Pearson correlation analysis. Third, the GWR model was introduced to analyze the causes of NTLIC from the perspective of nonstationarity characteristics. Fig. 3 shows the schematic flowchart of the proposed analytical framework.

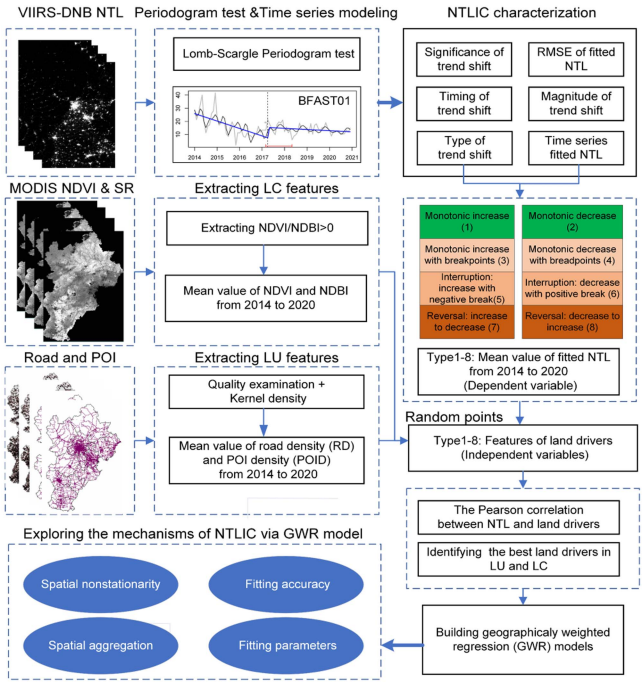

Fig. 3. Flowchart of the proposed analytical framework.

A. Lomb-Scargle Periodogram

Although some studies have reported the seasonal effects of monthly VIIRS-DNB NTL [3], [17], [30], it is necessary to verify whether there is an annual periodicity (i.e., 12 months) before utilizing the time series model. Therefore, the Lomb–Scargle periodogram algorithm was chosen to prove the existence of periodic components in the monthly VIIRS-DNB NTL time series [45]. This algorithm can detect weak periods, even if there are noises and gaps in the observed data [46]. This method is described mathematically as follows

$$PN(\omega) = \frac{1}{2\sigma^2}\left\{\frac{\left[\sum_i^n \left(Y_i - \bar{Y}\right)\cos\omega\left(t_i - \tau\right)\right]^2}{\sum_i^n \cos^2\omega\left(t_i - \tau\right)} + \frac{\left[\sum_i^n \left(Y_i - \bar{Y}\right)\sin\omega\left(t_i - \tau\right)\right]^2}{\sum_i^n \sin^2\omega\left(t_i - \tau\right)}\right\} \quad (2)$$

$$\tau = \left(\frac{1}{2\omega}\right)\tan^{-1}\left[\frac{\sum_i^n \sin 2\omega t_i}{\sum_i^n \cos 2\omega t_i}\right] \quad (3)$$

where Y_i, $\bar{Y}$ denote the observed NTL pixel value for $i = 1, 2, 3, \ldots, n$ and the mean of the data Y_i, respectively, and n is the observation number; t_i is the sampling time; σ^2 is the variance of the time series data; PN is the power normalized by σ^2; ω is the angular frequency of periods; and τ is a parameter used to adjust the phase shift caused by non-uniform sampling. Under the null hypothesis that the VIIRS-DNB NTL time series is aperiodic, the false-alarm probability (p) was computed (4) with the tested frequency (M)

$$p = 1 - \left(1 - e^{-PN}\right)^M \quad (4)$$

Before judging the presence of periodicity, we need to eliminate the influence of abnormal values [30]. Thus, pixels with zero values, the first and last 5th percentile of the observations, were masked out.

This method was applied to monthly VIIRS-DNB NTL data from 2014 to 2020 in Beijing. We chose Beijing as a test area because it has both high-intensity human activities and high vegetation cover [47], where seasonal characteristics of NTL are more likely to occur. In addition, urban and rural areas were identified by the Beijing Development Document in 2017 to analyze the difference in urban–rural NTL. The urban areas comprise six districts: Dongcheng, Xicheng, Chaoyang, Haidian, Fengtai, and Shijingshan. The remaining ten districts were considered rural areas.

B. Time Series Modeling of NTL Data

The BFAST01 model was adopted to detect the gradual and abrupt changes in the monthly VIIRS-DNB NTL data. It is a season-trend model that adequately accounts for typical change dynamics within the time series NTL data, including intra-annual (seasonality) and inter-annual (trend) changes. This model was proposed by Jong et al. [27] to assess the major changes of global NDVI in the long term. Meanwhile, this method could identify the breakpoints and the trend types. Compared to the BFAST model proposed by Verbesselt et al. [23], BFAST01 has been improved to detect the most significant trend change while ignoring minor shifts. In addition, BFAST01 fits the season and trend models simultaneously to save time during the fitting process.

The BFAST01 model decomposes the time series data into trend and seasonal signals with linear and harmonic functions, respectively. It is implemented as

$$y_t = \alpha + \beta t + \sum_{j=1}^{k} \gamma_j \sin\left(\frac{2\pi j t}{f} + \delta_j\right) + \varepsilon_t \quad (5)$$

where α and β are the intercept and slope of the trend, respectively; γ_j and δ_j are the amplitude and phase of seasons, respectively; f is the period of the time series ($f = 12$ for monthly VIIRS-DNB NTL); and ε_t is the noise or residual component when the observation time is t (with standard deviation σ). This article used three harmonic terms (i.e., $k = 3$) to effectively detect interferences [30] within monthly VIIRS-DNB NTL data. After fitting the model, the major breakpoint is identified by computing the moving sum of the residuals of ordinary least squares (OLS-MOSUM) of residuals at time t in the form of

$$\text{OLS} - \text{MOSU}\ M_t = \left\{\frac{1}{\hat{\sigma}\sqrt{[S.h]}} \times \sum_{i=t-[S.h]+1}^{t} \left(y_i - \hat{y}_i\right)\right\}_{t=[S.h]}^{S} \quad (6)$$

where S is the time series length. The value of $h \in (0, 1)$ is determined by the time series length and period length, which controls the minimum duration of the trend segment. Thus, $[S.h]$ indicates the length of the moving windows. y_i is the actual observation, and $\hat{y}_i$ is the fitted value, so $(y_i - \hat{y}_i)$ is the OLS

TABLE II
CHARACTERISTICS OF GRADUAL AND ABRUPT CHANGE TYPES IN BFAST01 MODEL

Type	Segment 1	Segment 2	Break	Group
1	Increasing	Increasing	NA	Monotonic
2	Decreasing	Decreasing	NA	Monotonic
3	Increasing	Increasing	Increasing	Monotonic
4	Decreasing	Decreasing	Decreasing	Monotonic
5	Increasing	Increasing	Decreasing	Interruption
6	Decreasing	Decreasing	Increasing	Interruption
7	Increasing	Decreasing	Decreasing	Reversal
8	Decreasing	Increasing	Increasing	Reversal

Note: the types with green color and orange color belong to gradual change and abrupt change, respectively.

residual. The standard deviation is $\hat{\sigma}$. If the time series data were stable, $\mathrm{OLS}-\mathrm{MOSUM}_t$ should fluctuate around zero. Conversely, if large fluctuations occur, $|\mathrm{OLS}-\mathrm{MOSUM}_t|$ will deviate from zero. If the significance level of the deviation at time t is more than 95%, an abrupt change will be detected and regarded as a breakpoint [48]. Furthermore, the magnitude of an abrupt change at a breakpoint is derived by the difference between $\alpha_1+\beta_1 t$ at t^*_{j-1} and t^*_j, so that

$$\text{Magnitude} = (\alpha_{j-1}-\alpha_j) + (\beta_{j-1}-\beta_j)\,t. \tag{7}$$

Then, the type of NTLIC was identified by the BFAST01 model. It divides the detection results into eight types, including two gradual changes and six abrupt changes. According to the characteristics of the change, the abrupt changes are divided into three groups, including monotonic changes, interruptions, and reversals (see Table II). The fitted NTL was the sum of two components, i.e., trend and seasonal signals.

C. Analysis of Land Drivers of NTLIC From a Spatial Nonstationary Perspective

The land features related to NTL were extracted from the time series of NDVI, NDBI, RD, and five types of POI density (POID) from 2014 and 2020. First, pixels with NDVI and NDBI values less than 0 were masked to leave areas with vegetation or built-up areas. Second, the road and POI vector data were subjected to quality inspection and kernel density analysis to produce a smooth RD and POID raster image of 500 m in each year. Third, all potential factors in raster form and the fitted NTL time series data were used to calculate the mean value for each pixel for seven years as the average intensity of land drivers and NTLIC at the pixel scale. We randomly selected 2278 vector points in the study area and extracted the mean values of each factor and fitted NTL. Then, Pearson correlation was performed to identify the most significant factors in the LC and LU terms. To better address the problem of the spatial heterogeneity of the primary land drivers of NTLIC, we examined their relationships using GWR. The GWR model was rewritten as follows:

$$y_i = \beta_0\ (u_i, v_i) + \sum\nolimits_k \beta_k\,(u_i, v_i)\,x_{ik} + \varepsilon_i \tag{8}$$

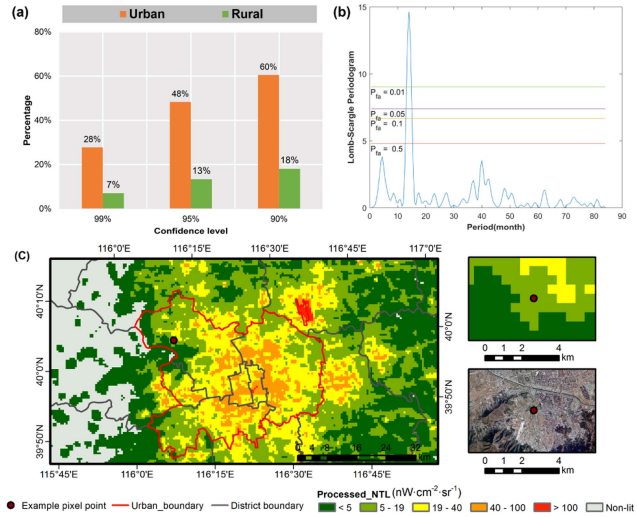

Fig. 4. (a) Percentage histogram with annual periodicity. (b) Example of this test with one significant periodicity detected. (c) Location of the example pixel point.

where (u_i, v_i) denotes the coordinates of the ith point in space, $\beta_0(u_i, v_i)$ is the intercept for location i, $\beta_k(u_i, v_i)$ represents the local parameter estimate for independent variable x_k at location i, and ε_i is the random error term at point i.

Compared to global parameter estimates, such as ordinary least squares regression (OLSR), GWR has higher accuracy because its estimates are not constant but vary over space [49]; therefore, it could help uncover the hidden causes of NTLIC.

IV. RESULTS

A. Lomb–Scargle Periodogram

The percentage histogram of the Lomb–Scargle periodogram test for the presence of a 12-month periodicity is shown in Fig. 4(a). In the urban area, 60%, 48%, and 28% of the VIIRS-DNB NTL time series showed an annual rhythm at the 90%, 95%, and 99% confidence levels, respectively. In contrast, the seasonal pattern of VIIRS-DNB NTL in rural areas was relatively weak. In addition, we selected a typical pixel located in the urban area of Beijing [see Fig. 4(c)] to verify the periodicity. Fig. 4(b) shows the significance of different seasonal information of this pixel. Only one significant periodicity was detected, i.e., 12 months, and the other two periodic patterns did not reach the 50% confidence level. In summary, there is indeed a 12-month periodicity in the monthly VIIRS-DNB NTL in Beijing, which is much more pronounced in urban areas than in rural areas.

B. Spatial Pattern of VIIRS-DNB NTL Data With Time-Series Modeling

Fig. 5 presents the spatial pattern of the fitted NTL from the BFAST01 model, the processed NTL in May 2020, and the RMSE of the fitted NTL in the whole time series over the BTH megaregion. To differentiate the NTL intensity, the natural break method was adopted to divide it into five ranks: lowest, lower,

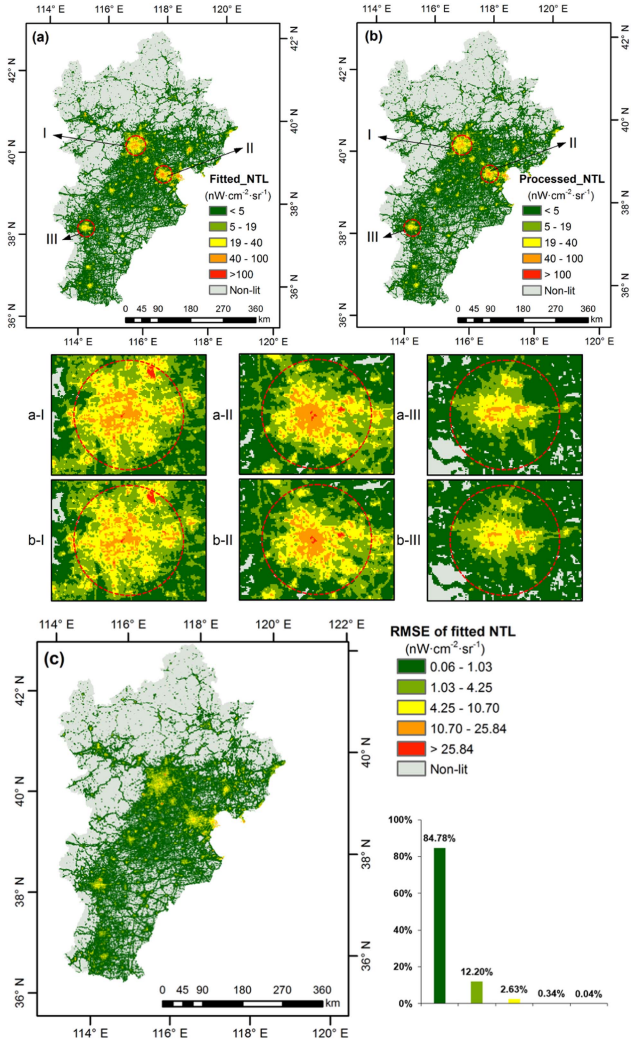

Fig. 5. Spatial pattern of (a) the fitted NTL from BFAST01, (b) the processed NTL in May 2020, and (c) the *RMSE* between the fitted NTL and the processed NTL from 2014 to 2020.

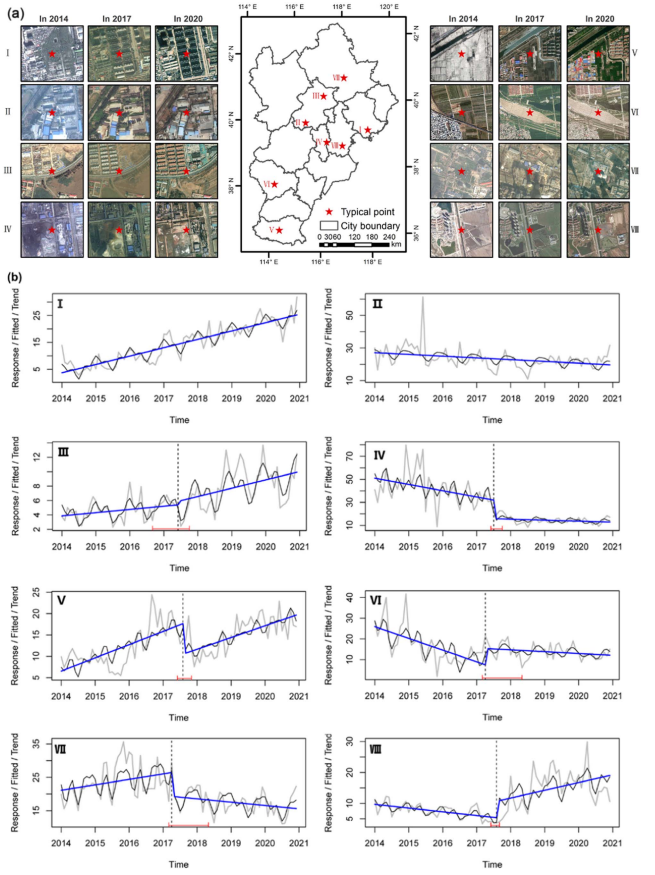

Fig. 6. Representative cases of the BFAST01 model output related to trend types. (a) Spatial distribution of high-spatial-resolution images and (b) temporal signatures of 8 samples; cases (I) and (II) are gradual changes that represent monotonic increase (type 1) and monotonic decrease (type 2), respectively; cases (III-VIII) belong to abrupt changes: Case (III) has a positive break in monotonic increase (type 3); case (IV) has a negative break in monotonic decrease (type 4); case (V) increases with setback after interruption (type 5); case (VI) decreases with burst after interruption (type 6); case (VII) reverses, which changes from increase to decrease (type 7); and VIII) reverses, which changes from decrease to increase (type 8). The horizontal red bar represents the confidence interval of the estimated time of the abrupt change. The gray, black, and blue lines represent the processed NTL, the fitted NTL, and trend components, respectively.

medium, higher, and highest level. The spatial pattern of the fitted NTL data was consistent with the processed NTL data [see Fig. 5(a) and (b)].

Notably, the fitted NTL data showed more homogeneous and less fragmented areas in the higher rank due to the smoothing effect of BFAST01 modeling. This shows that the fitted NTL of BFAST01 is more flexible in extracting the urban area and analyzing the intensity of human activities. Moreover, the *RMSE* of each pixel was mainly concentrated at the lowest level, ranging from 0.06 to 1.03 $nW \cdot cm^{-2} \cdot sr^{-1}$, accounting for 84.78% [see Fig. 5(c)]. Thus, the fitted NTL data after BFAST01 modeling significantly improved the spatial clustering of high-intensity NTL data.

C. NTLIC Characterization

1) Typical Analysis of NTLIC: To clarify the characterization of eight types of NTLIC (see Table II), eight typical cases were selected to compare urban landscapes and describe the temporal trajectories of VIIRS-DNB NTL (see Fig. 6). These cases covered seven cities, including Chengde, Beijing, Tangshan, Langfang, Tianjin, Shijiazhuang, and Handan, which showed differences in geographical location and socioeconomic development conditions. Fig. 6(a) shows the urban landscape changes in eight cases in the BTH megaregion from 2014 to 2020. Comparison of the high-spatial-resolution images revealed that most landscape structure and function changed significantly in these cases. On the one hand, natural surface, i.e., greenspace, bare land, and deserted land, was transformed into built-up area (in cases I, III, V, VI, and VII); on the other hand, the reverse direction of conversion, i.e., from built-up area to natural land, occurred in case VIII. These apparent changes in the land may lead to NTLIC appearing in diverse temporal trajectories. In addition, there were several minor changes or no changes in *LC,* but still with obvious NTLIC (in cases II and IV). That is, the NTLIC did not always coincide with the LC changes.

Fig. 6(b) illustrates eight cases of the BFAST01 model output, where the original time series data, the fitted curve, and the trend components are shown as gray, black, and blue lines,

respectively. Cases I and II denote monotonic increases and monotonic decreases, respectively. Cases of abrupt changes are represented in Fig. 6(b) (III–VIII). The vertical dashed line in these figures represents the time of the major abrupt change in the time series. From the temporal trajectories of eight cases, the trend of the fitted seasonal curve and trend line remained consistent with the processed NTL data. It mitigated the effect of noise, especially in cases II, IV, and V.

2) Regional Characteristics of NTLIC Trends: The NTLIC trends across the BTH megaregion exhibited evident spatial heterogeneity between 2014 and 2020 [see Fig. 7(a)]. A total of 63.35% of pixels were characterized by increasing trends (including the monotonic increase (positive break) and the increase with setback); these pixels were primarily located in central areas with a high economic level and flat terrain. A total of 22.46% of the pixels were characterized by a decrease to increase, with the breakpoints primarily distributed in the peripheral area with an undeveloped economy and higher terrain. The percentage of pixels characterized by increases to decreases was 6.61%. Pixels characterized by this type of trend change were mainly embedded in the area of monotonic increase. The results also revealed that only 4.37%, 0.20%, and 3.01% were characterized by a monotonic decrease (no break), monotonic decrease (negative break), and decrease with burst, respectively. These declining pixels were mainly located in the coastal areas.

From the timing of abrupt changes [see Fig. 7(b)], most pixels primarily occurred in April and August 2017, accounting for 32.80% and 12.71%, respectively. The remaining breakpoints (14.71%) occurred in May, June, and July 2017. In addition, the pixels characterized by significant trends only after the break (23.85%) were largely distributed in the rural regions of the southern and eastern areas [see Fig. 7(c)]. The magnitude of abrupt changes at a breakpoint for the time-series NTL is shown in Fig. 7(d). Most pixels (71.61%) had a magnitude from 0 to 2 $nW{\cdot}cm^{-2}{\cdot}sr^{-1}$ between two segments. These pixels were mainly distributed in the non-central urban and rural areas. Moreover, pixels with an absolute magnitude value of 4 $nW{\cdot}cm^{-2}{\cdot}sr^{-1}$ were less than 5%. These pixels were largely located in Beijing and its surrounding cities, i.e., Langfang and Tianjin.

In short, the dominant pixels with increasing trends (63.35%) were mainly located in the central cities and their neighborhoods, i.e., Beijing and Baoding, while the dominant pixels with decreasing trends (4.57%) primarily occurred in the coastal cities, i.e., Tianjin and Tangshan. Most abrupt changes (type 8, decrease to increase, 37.29% of the abrupt changes) were largely distributed in the peripheral cities, i.e., Handan and Shijiazhuang.

D. Causes of NTLIC From the Perspective of Spatial Nonstationarity

Table III gives the results of Pearson correlation analyses between the mean fitted NTL intensity and the mean value of eight factors from 2014 to 2020. Overall, the correlation between factors and NTL intensity was significant at the 0.01 (two- tailed) level. RD ($r = 0.693$) was the most important factor

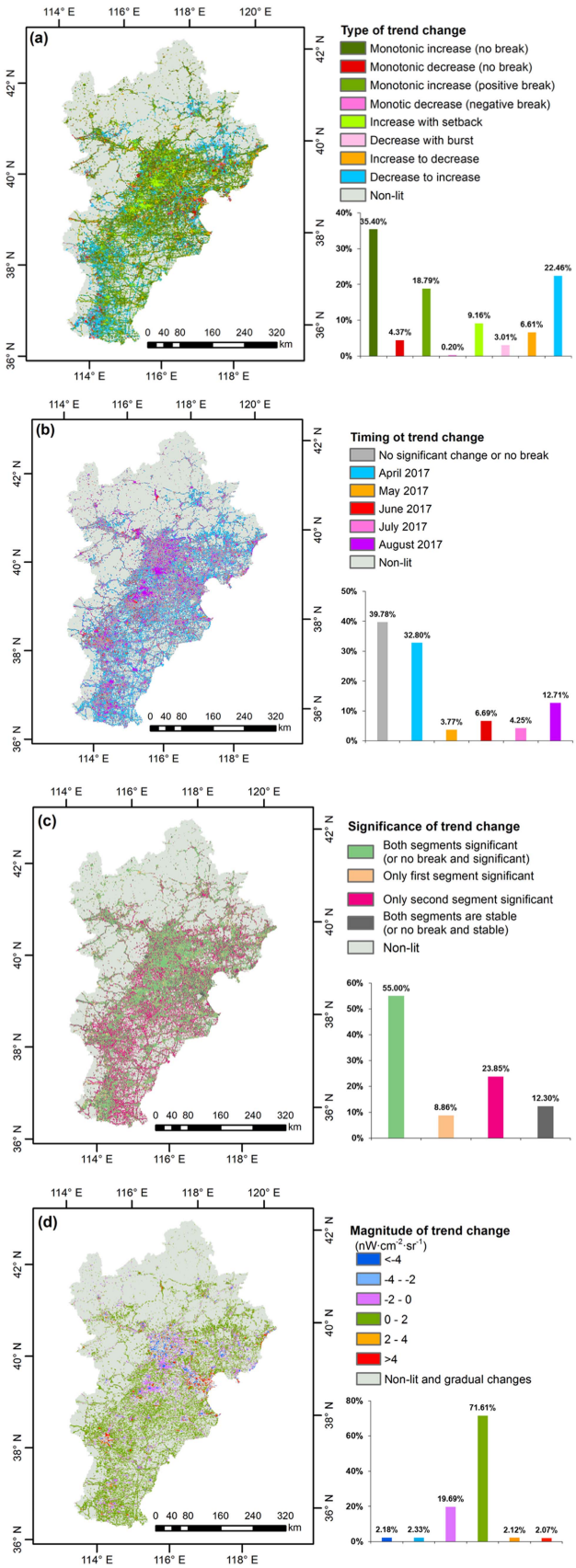

Fig. 7. (a) Type, (b) timing, (c) significance, and (d) magnitude of changes in the monthly VIIRS-DNB NTL intensity trend. The inset in each panel shows the percentage of pixels with interval values indicated by the color in the legend.

TABLE III
PEARSON CORRELATION ANALYSES BETWEEN NTL INTENSITY AND POTENTIAL LAND FACTORS

Factor	r	Factor	r
RD	0.693**	Industrial POID	0.498**
Residential POID	0.683**	Greenspaces POID	0.683**
Public POID	0.677**	NDVI	-0.338**
Commercial POID	0.688**	NDBI	0.224**

Note: **denotes the significance at the 0.01 (two-tailed) level.

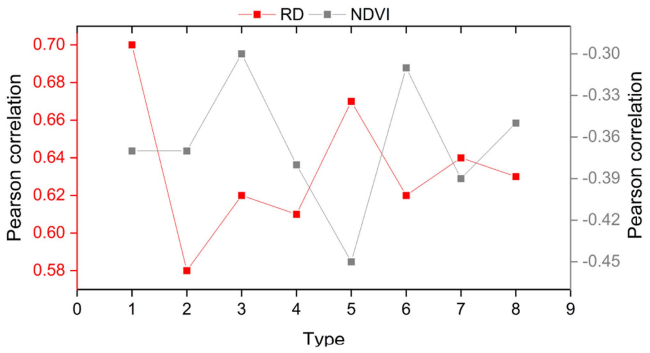

Fig. 8. Pearson correlation degree (r) between the NTL intensity and two factors (RD and NDVI) in eight types of the NTLIC (at the 0.01 significance level).

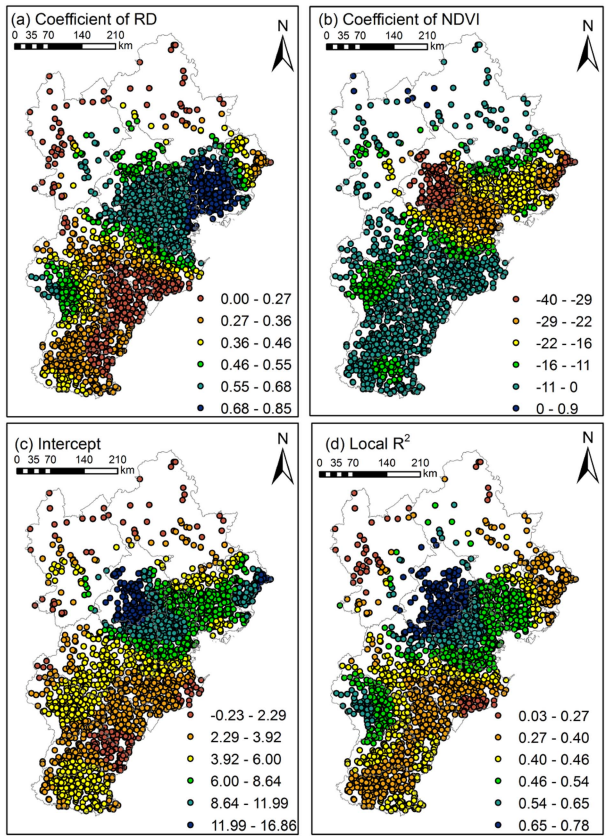

Fig. 9. Spatial variation of regression outputs from the GWR model for NTL and land drivers in the study area: (a) the coefficient of RD; (b) the coefficient of NDVI; (c) the intercept; and (d) local R^2.

in LU, and NDVI ($r = -0.338$) was the most significant factor in LC. Therefore, they were the optimal explanatory variables to explain NTLIC in eight types. As shown in Fig. 8, there are significant differences in the effects of NDVI and RD on NTL intensity among the eight types of NTLIC. The correlation between RD and NTL was positive, with an r-value ranging from 0.58 to 0.70. In comparison, the negative correlation between NDVI and NTL was much weaker, with an r-value ranging from -0.30 to -0.45. This illustrates the variability in the extent to which vegetation and roads contribute to NTL intensity in different NTLIC trends.

In this article, we used the GWR model to analyze the mechanisms of the NTLIC trends. The goodness of fit (R^2) of the GWR model was 0.60, implying that NDVI and RD could explain nearly 60% of NTLIC. Overall, the spatial nonstationarity and aggregation of the GWR model parameters, i.e., the coefficient of RD [see Fig. 9(a)], the coefficient of NDVI [see Fig. 9(b)], and the intercept [see Fig. 9(c)], were apparently shown. In the central cities and their nearby cities, such as Beijing, Tianjin, and Langfang, the contributions of RD and NDVI were both higher [see Fig. 9(a) and (b)]. Thus, the mean value of local R^2 in these three cities was higher (>0.53) (see Table IV). However, in the northern and southeastern parts of the study area, the local R^2 values were lower [see Fig. 9(d)], indicating that other factors had more influence on the NTLIC trends. The spatial pattern of local R^2 represented a decreasing trend with increasing distance from the central cities [see Fig. 9(d)]. Moreover, the relationship between NDVI and NTL was more complicated than that between RD and NTL because of two points: the spatial heterogeneity of the effect of NDVI on NTL [see Fig. 9(b)] was more obvious than that of RD, especially in central areas; and the correlation between NDVI and NTL included strong negative and weak positive effects, whereas that of RD and NTL maintained only a positive relationship.

TABLE IV
REGRESSION LOCAL R^2 OF GWR IN 13 CITIES OF THE STUDY AREA

City	Min local R^2	Max local R^2	Mean local R^2
Baoding	0.35	0.74	0.49
Beijing	0.56	0.78	0.73
Cangzhou	0.22	0.50	0.36
Chengde	0.06	0.68	0.38
Handan	0.37	0.41	0.39
Hengshui	0.30	0.44	0.38
Langfang	0.40	0.72	0.59
Qinhuangdao	0.30	0.41	0.34
Shijiazhuang	0.40	0.61	0.51
Tangshan	0.35	0.51	0.47
Tianjin	0.48	0.67	0.54
Xingtai	0.38	0.50	0.41
Zhangjiakou	0.03	0.71	0.29

TABLE V
STATISTICS OF ANNUAL FITTED NTL INTENSITY VIA BFAST01 IN THE BTH MEGAREGION

Year	Mean ($nW{\cdot}cm^{-2}{\cdot}sr^{-1}$)	STD ($nW{\cdot}cm^{-2}{\cdot}sr^{-1}$)	CV
2014	2.45	6.16	2.52
2015	2.57	6.27	2.44
2016	2.69	6.50	2.42
2017	2.89	6.70	2.32
2018	3.11	6.93	2.23
2019	3.36	7.28	2.17
2020	3.60	7.82	2.17

Note: STD (standard deviation) and CV (coefficient of variation).

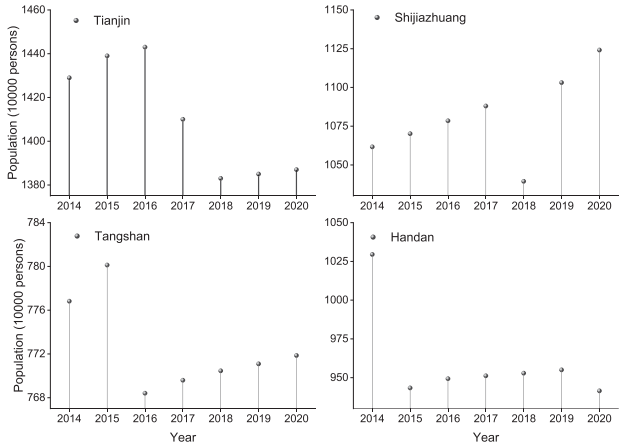

Fig. 10. Total permanent population changes from 2014 to 2020 in Tianjin, Shijiazhuang, Tangshan, and Handan.

V. DISCUSSION

A. Gradual and Abrupt Changes in Monthly VIIRS-DNB NTL and Their Links With Urbanization

The results of time-series NTL analysis by the BFAST01 model show some characteristics in the spatial and temporal urbanization trajectories. First, there are different temporal trajectories of urbanization, which are distinguishable from the trends of the NTLIC (see Fig. 7). Eight types of NTL trajectories present the directions and forms of urbanization. In the gradual changes, type 1 (monotonic increase) and type 2 (monotonic decrease) can indicate urban growth and deurbanization [6]. Six trend types of abrupt changes imply the diversity and complexity of urbanization. Thus, the causes of the monthly abrupt changes were complicated, i.e., environmental disturbances (fires and floods) on the land surface [50] and human interventions in the urbanization process, i.e., the large-scale urban transformation of old buildings and factories [51]. It is important to note that the types of abrupt changes identified in this study based on monthly average NTL composites may include the effects of short-term events (such as power outages) on NTL intensity. In this condition, we should pay more attention to these areas with abrupt changes, especially in two inverse types (types 7 and 8, increase to decrease and decrease to increase).

From Fig. 7(a), we can identify the spatial characteristics of NTLIC. First, most areas (63.35%) in the BTH megaregion experienced urbanization growth, which could illustrate the effectiveness of the national urban development policy to some extent. Some researchers have shown that coordinated regional development and redistribution of noncapital functions are important policies of the BTH megaregion between 2014 and 2020 [52]. Moreover, the average intensity of annual fitted NTL has improved from 2.45 to 3.60 $nW{\cdot}cm^{-2}{\cdot}sr^{-1}$, while the coefficient of variation (CV) of NTL intensity has decreased from 2.52 to 2.12 during this period (see Table V). Overall, the urbanization process in the BTH megaregion is growing, and intraregional disparities are narrowing.

TABLE VI
VALIDATION POINTS FOR INSPECT THE LC AT THE BREAKPOINT TIME OF THE ABRUPT CHANGES

Abrupt_ type	Total number	Num_c	Num_s	Ratio_c (%)	Ratio_s (%)
3	56	8	48	14.29	85.71
4	65	20	45	30.77	69.23
5	70	20	50	28.57	71.43
6	69	16	53	23.19	76.81
7	68	19	49	27.94	72.06
8	58	12	46	20.69	79.31

Note: total number denotes the total number of six types of abrupt changes. Num_c and num_s denote the number of change pixels and the same pixels in LC, respectively; ratio_c and ratio_s denote ratio of change pixels and the same pixels in LC to the total number, respectively. The type codes are according to Table II.

Second, the highlighted areas of the BTH megaregion in the coastal and peripheral cities, i.e., Tianjin, Tangshan, Shijiazhuang, and Handan, were in deurbanization and unstable urbanization and need to make appropriate regulations to improve their development. The population changes in these four cities during the same period also show sharp declines or significant fluctuations (see Fig. 10). Moreover, the areas with severely decreasing NTL trends (magnitude $< -4\ nW{\cdot}cm^{-2}{\cdot}sr^{-1}$) were mainly located in the rural areas of Beijing, Langfang, and Tangshan [see Fig. 7(d)]. Therefore, these regions deserve more attention in the BTH megaregion.

It is interesting that the timing of abrupt NTL changes was all in 2017. We indirectly validated the effectiveness of breakpoint time of NTL by judging the LC changes at the time of abrupt NTLIC. In Table VI, the daytime changes of LC did not coincide well with the NTLIC because the ratio of change pixels in LC was less than 35%. This phenomenon could be seen in Fig. 6(a), where some locations, such as abandoned factories, did not show obvious LU changes, but showed a major decrease in NTL intensity due to population loss. Moreover, the average NTL value ($3.49\ nW{\cdot}cm^{-2}{\cdot}sr^{-1}$) of the pixels with the original LC condition was lower than that of the pixels with LC changes ($5.74\ nW{\cdot}cm^{-2}{\cdot}sr^{-1}$). This may indicate that the pixels with both

TABLE VII
LOCAL R^2 OF GWR IN EIGHT TYPES OF NTLIC

Type	Min local R^2	Max local R^2	Mean local R^2
1	0.03	0.78	0.48
2	0.27	0.76	0.49
3	0.10	0.77	0.46
4	0.33	0.45	0.39
5	0.31	0.77	0.54
6	0.31	0.76	0.47
7	0.04	0.77	0.47
8	0.07	0.78	0.45

LC changes and NTLIC were mainly distributed in the urban areas with high intensity of human activities. The other important reason was that 2017 was the crucial year to implement the coordinated regional development and redistribution of non-capital functions in the BTH megaregion [53]. The implementation of urban policies not only results in the LC changes, but could also lead to changes in urban functions, human activities, and population migration [7]. These changes are difficult to detect directly from daytime remote sensing images. Therefore, it was valuable to further investigate the causes of NTLIC.

B. Performance of GWR to Reveal the Response Process of NTLIC

Combining the results of GWR (see Fig. 9 and Table IV), the NTLIC trend in response to land drivers is a spatial nonstationary process, and the variations in space can change the mechanism of response of NTL to land drivers. The performance of GWR had an R^2 value of 0.60, which outperformed the ability of OLSR with an R^2 value of 0.49. Generally, the higher RD led to stronger NTL intensity in the study area because the relationship between them was positive. Moreover, this positive effect was much stronger in the central cities than in other areas. In contrast, the higher NDVI did not result in lower NTL intensity, especially in northern areas. Both negative and positive effects complicated the relationship between NDVI and NTL intensity. Some studies also found this condition on a large scale [54], [55]. It is worthwhile to improve the positive effects of NDVI on NTL through urban planning methods in the central areas.

The local R^2 of GWR in different types of NTLIC also showed apparent variability (see Table VII). From the mean level of local R^2, types 1 (monotonic increase), 2 (monotonic decrease), and 5 (increase with setback) had higher values (R^2 >0.47). These three types of NTLIC were mainly located in central cities and their surrounding areas [see Fig. 7(a)], which presented higher levels of urbanization. Therefore, the patterns of NTLIC trends and their response mechanisms showed significant spatial heterogeneity and aggregation characteristics.

C. Implication for Sustainable Urbanization in the BTH Megaregion

NTL intensity is an effective proxy for human activities and helps us to better understand urbanization. Combined with the spatial characteristics of the NTLIC and its main drivers, three implications for promoting urban sustainability were suggested. First, central cities should increase the vegetation cover in the downtown area to improve the positive effect of vegetation on NTLIC. For example, the renewal of old villages and towns could emphasize more public greenspaces around buildings to improve the environmental quality. Second, coastal, and peripheral cities should strengthen road infrastructure to improve mobility of socio-economic activities with surrounding cities. This suggestion was consistent with the strong positive effect of RD on the NTLIC. Third, coastal cities should adjust their industrial structure to take full advantage of the sea, such as strengthening the development of seaside tourism or other forms of port economic development.

VI. CONCLUSION

This article adopted the BFAST01 algorithm to characterize the monthly gradual and abrupt changes in NTL intensity from 2014 to 2020 and the GWR model to investigate the relationships between the NTLIC and land drivers from the perspective of nonstationarity, taking the BTH megaregion of China as the study area. The results show that: there was significant spatial heterogeneity in the NTLIC pattern; the increasing trends (63.35%) and decreasing trends (4.57%) were mainly located in central cities and coastal cities, respectively; the dominant abrupt changes (type 8) occurred primarily in April 2017; in the GWR model, RD and NDVI could explain 60% of the NTLIC, which outperformed the performance of OLSR ($R^2 = 0.49$); and the relationship between the NTLIC and land drivers showed significant spatial heterogeneity and aggregation characteristics. This article reveals the monthly NTL intensity dynamics and its internal mechanism, providing novel knowledge into the usage of time-series NTL images to characterize urbanization and driving factors of NTL trends.

ACKNOWLEDGMENT

The authors thank the reviewers and editors for their constructive comments and suggestions.

REFERENCES

[1] M. M. Bennett and L. C. Smith, "Advances in using multitemporal night-time lights satellite imagery to detect, estimate, and monitor socioeconomic dynamics," *Remote Sens. Environ.*, vol. 192, pp. 176–197, Apr. 2017.
[2] N. Levin et al., "Remote sensing of night lights: A review and an outlook for the future," *Remote Sens. Environ.*, vol. 237, Feb. 2020, Art. no. 111443.
[3] Z. Chen et al., "Delineating seasonal relationships between Suomi NPP-VIIRS nighttime light and human activity across Shanghai, China," *IEEE J. Sel. Topics Appl. Earth Observ. Remote Sens.*, vol. 12, no. 11, pp. 4275–4283, Nov. 2019.
[4] C. D. Elvidge et al., "Night-time lights of the world: 1994–1995," *Int. Soc. Photogramm. Remote Sens. J. Photogramm. Remote Sens.*, vol. 56, no. 2, pp. 81–99, Dec. 2001.

[5] N. Levin and Q. Zhang, "A global analysis of factors controlling VIIRS nighttime light levels from densely populated areas," *Remote Sens. Environ.*, vol. 190, pp. 366–382, 2017.

[6] Q. Zhang and K. C. Seto, "Mapping urbanization dynamics at regional and global scales using multi-temporal DMSP/OLS nighttime light data," *Remote Sens. Environ.*, vol. 115, no. 9, pp. 2320–2329, Sep. 2011.

[7] Q. Zheng, Q. Weng, and K. Wang, "Characterizing urban land changes of 30 global megacities using nighttime light time series stacks," *Int. Soc. Photogramm. Remote Sens. J. Photogramm. Remote Sens.*, vol. 173, pp. 10–23, 2021.

[8] H. Bagan and Y. Yamagata, "Analysis of urban growth and estimating population density using satellite images of nighttime lights and land-use and population data," *GISci. Remote Sens.*, vol. 52, no. 6, pp. 765–780, Nov. 2015.

[9] P. Sutton, D. Roberts, C. Elvidge, and K. Baugh, "Census from heaven: An estimate of the global human population using night-time satellite imagery," *Int. J. Remote Sens.*, vol. 22, no. 16, pp. 3061–3076, Nov. 2001.

[10] J. V. Henderson, A. Storeygard, and D. N. Weil, "Measuring economic growth from outer space," *Amer. Econ. Rev.*, vol. 102, no. 2, pp. 994–1028, 2012.

[11] T. Ma, Y. Zhou, C. Zhou, S. Haynie, T. Pei, and T. Xu, "Night-time light derived estimation of spatio-temporal characteristics of urbanization dynamics using DMSP/OLS satellite data," *Remote Sens. Environ.*, vol. 158, pp. 453–464, Mar. 2015.

[12] C. D. Elvidge et al., "A fifteen year record of global natural gas flaring derived from satellite data," *Energies*, vol. 2, no. 3, pp. 595–622, 2009.

[13] Y. Zhou, X. Li, G. R. Asrar, S. J. Smith, and M. Imhoff, "A global record of annual urban dynamics (1992–2013) from nighttime lights," *Remote Sens. Environ.*, vol. 219, pp. 206–220, Dec. 2018.

[14] Q. Zheng, Q. Weng, Y. Zhou, and B. Dong, "Impact of temporal compositing on nighttime light data and its applications," *Remote Sens. Environ.*, vol. 274, Jun. 2022, Art. no. 113016.

[15] M. M. Bennett and L. C. Smith, "Using multitemporal night-time lights data to compare regional development in Russia and China, 1992–2012," *Int. J. Remote Sens.*, vol. 38, no. 21, pp. 5962–5991, Nov. 2017.

[16] Y. Xie, Q. Weng, and P. Fu, "Temporal variations of artificial nighttime lights and their implications for urbanization in the conterminous United States, 2013–2017," *Remote Sens. Environ.*, vol. 225, pp. 160–174, May 2019.

[17] N. Levin, "The impact of seasonal changes on observed nighttime brightness from 2014 to 2015 monthly VIIRS DNB composites," *Remote Sens. Environ.*, vol. 193, pp. 150–164, May 2017.

[18] N. Zhao et al., "Time series analysis of VIIRS-DNB nighttime lights imagery for change detection in urban areas: A case study of devastation in Puerto Rico from hurricanes Irma and Maria," *Appl. Geography*, vol. 120, Jul. 2020, Art. no. 102222.

[19] X. Li, D. Li, H. Xu, and C. Wu, "Intercalibration between DMSP/OLS and VIIRS night-time light images to evaluate city light dynamics of Syria's major human settlement during Syrian Civil War," *Int. J. Remote Sens.*, vol. 38, no. 21, pp. 5934–5951, Nov. 2017.

[20] G. Xu, T. Xiu, X. Li, X. Liang, and L. Jiao, "Lockdown induced night-time light dynamics during the COVID-19 epidemic in global megacities," *Int. J. Appl. Earth Observ. Geoinf.*, vol. 102, Oct. 2021, Art. no. 102421.

[21] S. Liu, X. Li, N. Levin, and M. Jendryke, "Tracing cultural festival patterns using time-series of VIIRS monthly products," *Remote Sens. Lett.*, vol. 10, no. 12, pp. 1172–1181, Dec. 2019.

[22] C. Zhang, Y. Pei, J. Li, Q. Qin, and J. Yue, "Application of luojia 1-01 nighttime images for detecting the light changes for the 2019 spring festival in western cities, China," *Remote Sens.*, vol. 12, no. 9, Apr. 2020, Art. no. 1416.

[23] J. Verbesselt, R. Hyndman, G. Newnham, and D. Culvenor, "Detecting trend and seasonal changes in satellite image time series," *Remote Sens. Environ.*, vol. 114, no. 1, pp. 106–115, Jan. 2010.

[24] R. E. Kennedy, Z. Yang, and W. B. Cohen, "Detecting trends in forest disturbance and recovery using yearly Landsat time series: 1. LandTrendr—Temporal segmentation algorithms," *Remote Sens. Environ.*, vol. 114, no. 12, pp. 2897–2910, Dec. 2010.

[25] Z. Zhu and C. E. Woodcock, "Continuous change detection and classification of land cover using all available Landsat data," *Remote Sens. Environ.*, vol. 144, pp. 152–171, Mar. 2014.

[26] M. Reba and K. C. Seto, "A systematic review and assessment of algorithms to detect, characterize, and monitor urban land change," *Remote Sens. Environ.*, vol. 242, Jun. 2020, Art. no. 111739.

[27] R. De Jong, J. Verbesselt, A. Zeileis, and M. E. Schaepman, "Shifts in global vegetation activity trends," *Remote Sens.*, vol. 5, no. 3, pp. 1117–1133, Mar. 2013.

[28] L. Li, Y. Zhang, Q. Liu, M. Ding, and P. P. Mondal, "Regional differences in shifts of temperature trends across China between 1980 and 2017," *Int. J. Climatol.*, vol. 39, no. 3, pp. 1157–1165, Mar. 2019.

[29] F. Brakhasi, M. Hajeb, T. Mielonen, A. Matkan, and J. Verbesselt, "Investigating aerosol vertical distribution using CALIPSO time series over the Middle East and North Africa (MENA), Europe, and India: A BFAST-based gradual and abrupt change detection," *Remote Sens. Environ.*, vol. 264, Oct. 2021, Art. no. 112619.

[30] Q. Zheng, Q. Weng, and K. Wang, "Developing a new cross-sensor calibration model for DMSP-OLS and Suomi-NPP VIIRS night-light imageries," *Int. Soc. Photogramm. Remote Sens. J. Photogramm. Remote Sens.*, vol. 153, pp. 36–47, Jul. 2019.

[31] E. Guk and N. Levin, "Analyzing spatial variability in night-time lights using a high spatial resolution color Jilin-1 image – Jerusalem as a case study," *Int. Soc. Photogramm. Remote Sens. J. Photogramm. Remote Sens.*, vol. 163, pp. 121–136, May 2020.

[32] X. Li, L. Ge, and X. Chen, "Quantifying contribution of land use types to nighttime light using an unmixing model," *IEEE Geosci. Remote Sens. Lett.*, vol. 11, no. 10, pp. 1667–1671, Oct. 2014.

[33] C. Wang et al., "Analyzing parcel-level relationships between Luojia 1-01 nighttime light intensity and artificial surface features across Shanghai, China: A comparison with NPP-VIIRS data," *Int. J. Appl. Earth Observ. Geoinf.*, vol. 85, Mar. 2020, Art. no. 101989.

[34] J. Wu, Y. Tu, Z. Chen, and B. Yu, "Analyzing the spatially heterogeneous relationships between nighttime light intensity and human activities across Chongqing, China," *Remote Sens.*, vol. 14, no. 22, Nov. 2022, Art. no. 5695.

[35] Q. Zhang, C. Schaaf, and K. C. Seto, "The vegetation adjusted NTL urban index: A new approach to reduce saturation and increase variation in nighttime luminosity," *Remote Sens. Environ.*, vol. 129, pp. 32–41, Feb. 2013.

[36] B. Guo, Y. Fu, D. Hu, G. Zhang, and X. Wang, "Intercalibration of Luojia1-01 and Suomi-NPP-VIIRS monthly nighttime light composite using a spatial-temporal residuals correction random forest model," *IEEE J. Sel. Topics Appl. Earth Observ. Remote Sens.*, vol. 15, pp. 7712–7723, 2022.

[37] Z. Yang, H. Yang, and H. Wang, "Evaluating urban sustainability under different development pathways: A case study of the Beijing-Tianjin-Hebei region," *Sustain. Cities Soc.*, vol. 61, Oct. 2020, Art. no. 102226.

[38] M. Jiang, Y. He, C. Song, Y. Pan, T. Qiu, and S. Tian, "Disaggregating climatic and anthropogenic influences on vegetation changes in Beijing-Tianjin-Hebei region of China," *Sci. Total Environ.*, vol. 786, Sep. 2021, Art. no. 147574.

[39] Y. Ren and Z. Li, "Unraveling the dynamics, heterogeneity, determinants of eco-efficiency in Beijing-Tianjin-Hebei urban agglomeration, China," *J. Environ. Manage.*, vol. 317, Sep. 2022, Art. no. 115407.

[40] W. Ma, G. Jiang, Y. Chen, Y. Qu, T. Zhou, and W. Li, "How feasible is regional integration for reconciling land use conflicts across the urban–rural interface? Evidence from Beijing–Tianjin–Hebei metropolitan region in China," *Land Use Policy*, vol. 92, Mar. 2020, Art. no. 104433.

[41] M. Xu and Z. Zhang, "Spatial differentiation characteristics and driving mechanism of rural-industrial land transition: A case study of Beijing-Tianjin-Hebei region, China," *Land Use Policy*, vol. 102, Mar. 2021, Art. no. 105239.

[42] C. D. Elvidge, K. Baugh, M. Zhizhin, F. C. Hsu, and T. Ghosh, "VIIRS night-time lights," *Int. J. Remote Sens.*, vol. 38, no. 21, pp. 5860–5879, Nov. 2017.

[43] C. D. Elvidge, M. Zhizhin, T. Ghosh, F. C. Hsu, and J. Taneja, "Annual time series of global VIIRS nighttime lights derived from monthly averages: 2012 to 2019," *Remote Sens.*, vol. 13, no. 5, pp. 1–14, Mar. 2021.

[44] C. Xia, A. G. O. Yeh, and A. Zhang, "Analyzing spatial relationships between urban land use intensity and urban vitality at street block level: A case study of five Chinese megacities," *Landscape Urban Plan.*, vol. 193, Jan. 2020, Art. no. 103669.

[45] T. Ruf, "The Lomb-Scargle periodogram in biological rhythm research: Analysis of incomplete and unequally spaced time-series," *Biol. Rhythm Res.*, vol. 30, no. 2, pp. 178–201, 1999.

[46] J. D. Scargle, "Studies in astronomical time series analysis. II. Statistical aspects of spectral analysis of unevenly spaced data," *Astrophys. J.*, vol. 263, pp. 835–853, Dec. 1982.

[47] L. Huilei, P. Jian, L. Yanxu, and H. Yi'na, "Urbanization impact on landscape patterns in Beijing City, China: A spatial heterogeneity perspective," *Ecol. Indicators*, vol. 82, pp. 50–60, Nov. 2017.

[48] J. Verbesselt, A. Zeileis, and M. Herold, "Near real-time disturbance detection using satellite image time series," *Remote Sens. Environ.*, vol. 123, pp. 98–108, Aug. 2012.

[49] Z. Zhao, J. Gao, Y. Wang, J. Liu, and S. Li, "Exploring spatially variable relationships between NDVI and climatic factors in a transition zone using geographically weighted regression," *Theor. Appl. Climatol.*, vol. 120, no. 3/4, pp. 507–519, May 2015.
[50] Y. Zheng et al., "Rapid assessment of a typhoon disaster based on NPP-VIIRS DNB daily data: The case of an urban agglomeration along western Taiwan straits, China," *Remote Sens.*, vol. 11, no. 14, Jul. 2019, Art. no. 1709.
[51] X. Li, E. C. M. Hui, T. Chen, W. Lang, and Y. Guo, "From Habitat III to the new urbanization agenda in China: Seeing through the practices of the 'three old renewals' in Guangzhou," *Land Use Policy*, vol. 81, pp. 513–522, Feb. 2019.
[52] W. Yu and W. Zhou, "Spatial pattern of urban change in two Chinese megaregions: Contrasting responses to national policy and economic mode," *Sci. Total Environ.*, vol. 634, pp. 1362–1371, Sep. 2018.
[53] W. Jili and Y. Ming, "From 'redistribution'to 'optimization': Review of Beijing's non-capital function redistribution from 2009 to 2020," *Urban Devlop. Stud.*, vol. 27, no. 12, pp. 29–37, 2020.
[54] J. Du, Q. Fu, S. Fang, J. Wu, P. He, and Z. Quan, "Effects of rapid urbanization on vegetation cover in the metropolises of China over the last four decades," *Ecol. Indicators*, vol. 107, Dec. 2019, Art. no. 105458.
[55] Y. Liu et al., "correlations between urbanization and vegetation degradation across the world's metropolises using DMSP/OLS nighttime light data," *Remote Sens.*, vol. 7, no. 2, pp. 2067–2088, Feb. 2015.

Biyun Guo is currently working toward the Ph.D. degree in cartography and geography information system with Capital Normal University, Beijing, China.

Her research interests include nighttime light remote sensing and its application in urban research.

Deyong Hu received the Ph.D. degree in geographical information science (GIS) from Beijing Normal University, Beijing, China, in 2007.

He is currently a Professor of GIS with Capital Normal University, Beijing, China. His research interests include urban remote sensing and natural disaster remote sensing monitoring and evaluation.

Zongyao Wang is currently working toward the master's degree in cartography and geography information system with Capital Normal University, Beijing, China.

His research interests include urban environment and remote sensing.

Aixuan Lin is currently working toward the master's degree in cartography and geographic information system with Capital Normal University, Beijing, China.

Her research interests include nighttime light remote sensing and urban remote sensing.